applied sciences

Article

A Portable D-Shaped POF-SPR Sensor Integrated with NanoMIPs for High-Affinity Detection of the SARS-CoV-2 RBD Protein

Alice Marinangeli [1,*,†], Jessica Brandi [1,*,†], Devid Maniglio [2] and Alessandra Maria Bossi [1]

[1] Department of Biotechnology, University of Verona, Strada Le Grazie 15, 37134 Verona, Italy; alessandramaria.bossi@univr.it

[2] Department of Industrial Engineering, BIOtech Research Center, University of Trento, Via delle Regole 101, 38123 Trento, Italy; devid.maniglio@unitn.it

[*] Correspondence: alice.marinangeli@univr.it (A.M.); jessica.brandi@univr.it (J.B.); Tel.: +39-045-8027833 (A.M.); +39-045-8027874 (J.B.)

[†] These authors contributed equally to this work.

Abstract

The rapid and accurate detection of SARS-CoV-2 biomarkers remains a critical requirement for effective outbreak control and decentralized diagnostics. Although RT-PCR is the current gold standard, its reliance on centralized laboratories and long processing times limits its applicability in point-of-care settings. In this context, optical biosensing platforms based on surface plasmon resonance (SPR) offer attractive features, including label-free, real-time, and quantitative detection. This study explores the use of synthetic receptors for the highly sensitive detection of the receptor-binding domain (RBD) of the SARS-CoV-2 spike protein. Specifically, soft molecularly imprinted polymer nanoparticles (nanoMIPs) were employed as synthetic receptors and integrated into a high-sensitivity, portable plasmonic platform based on a D-shaped plastic optical fiber (POF) SPR sensor. The nanoMIPs were selectively imprinted against the RBD, characterized by Dynamic Light Scattering (DLS), Isothermal Titration Calorimetry (ITC), and Scanning Electron Microscopy (SEM) to confirm nanoMIPs size, binding properties, and surface morphology. Next, the nanoMIPs were immobilized onto a gold-coated sensing surface, enabling enhanced specificity, affinity, and signal amplification compared to conventional biological recognition elements. The resulting RBD-SPR-nanoMIPs sensor demonstrated promising analytical performance, exhibiting high selectivity against potentially interfering proteins and an anticipated sensitivity suitable for RBD detection at femtomolar concentrations. The inherent stability of nanoMIPs suggests the potential for reusable SPR sensing platforms, paving the way for next-generation synthetic receptor-based plasmonic biosensors.

Keywords: SARS-CoV-2; surface plasmon resonance (SPR); molecularly imprinted polymers (MIPs); portable sensor; D-shaped POF-SPR sensor

Check for updates

Academic Editor: Gang Wei

Received: 20 January 2026
Revised: 10 February 2026
Accepted: 11 February 2026
Published: 12 February 2026

1. Introduction

Severe acute respiratory syndrome coronavirus 2 (SARS-CoV-2) is a positive-sense, single-stranded RNA virus whose entry into host cells is mediated by the glycosylation of the spike (S) protein [1]. The receptor-binding domain (RBD) of the S protein is essential for viral attachment and entry and therefore represents a prime target for therapeutic and diagnostic applications [2,3].

https://doi.org/10.3390/app16041853

The COVID-19 pandemic highlighted the importance of developing rapid and reliable diagnostic tools [4,5]. Although RT-PCR remains the gold standard due to its high sensitivity, its reliance on time-consuming amplification steps and centralized laboratories limits its applicability for point-of-care testing [6,7].

To address these limitations, a wide range of biosensing platforms has been explored, including electrochemical, nucleic-acid-based, physical transduction, optical and plasmonic techniques [8,9]. For instance, magnetoelastic immunosensors have demonstrated rapid SARS-CoV-2 detection in complex matrices such as bioaerosols, highlighting the potential of alternative label-free sensing strategies [10].

Surface plasmon resonance (SPR) is widely employed as a label-free method for real-time monitoring of biomolecular interactions, combining rapid response with high sensitivity in applications related to SARS-CoV-2 detection [11,12]. Moreover, SPR enables the evaluation of binding kinetics, such as association and dissociation rates and affinity constants of antigen–antibody interactions [13]. In addition, its compatibility with different recognition strategies makes it particularly suitable for integrating innovative materials for portable and point-of-care devices [14–16].

SPR platforms combined with MIPs have been proposed to selectively recognize SARS-CoV-2 antigens, offering a promising approach toward low-cost, portable, and point-of-care diagnostic devices [17–20].

Molecularly imprinted polymers (MIPs) are synthetic receptors obtained via template-assisted polymerization, offering high selectivity, chemical stability, and cost-effectiveness compared to biological receptors [21–23]. The synthesis of MIPs typically involves the copolymerization of monomers and a cross-linker in the presence of a template molecule, followed by template removal, which leaves imprinted binding sites complementary in size, shape, and chemical functionalities to the target molecule [24,25].

MIPs can be synthesized in the format of a nanolayer, with a thickness of a few nm, or nanoparticles ("nanoMIPs" or "plastic antibodies"), typically with a diameter ranging from 10 to 500 nm [26]. Nanoformats with high surface-to-volume ratios ensure rapid mass-transfer kinetics, while their chemistry can be precisely controlled, allowing the design of responsive or functional materials [27,28]. When used to functionalize SPR sensors, these soft nanoMIPs can generate significant refractive index changes upon target binding, thereby enhancing sensor performance [29–32].

Concerning nanolayer-based approaches, previous studies developed an SPR sensor based on a D-shaped plastic optical fiber (POF) transducer functionalized with an acrylamide-based MIP nanolayer designed to selectively recognize the SARS-CoV-2 spike protein S1 subunit. Preliminary tests on nasopharyngeal swab samples yielded higher sensitivity and faster response times compared to conventional RT-PCR methods [31].

Moreover, a recent work presented a peptide epitope-imprinted polymer microarray for the selective recognition of the SARS-CoV-2 RBD. This design relied on imprinting a short peptide sequence (epitope) derived from the RBD onto a polyscopoletin nanofilm, yielding binding sites with dissociation constants in the low nanomolar range. Together, these features explain the superior analytical performance of nanoMIPs in SPR-based virus sensing [33].

NanoMIP-based SPR sensors can detect whole SARS-CoV-2 virus particles with high affinity, good sensitivity and strong specificity, compared to traditional MIP nano-films. Indeed nanoMIPs provide greater accessible surface area, faster and stronger binding signals, less diffusion limitation, and improved reproducibility and stability. Together, these features explain why nanoMIPs yield higher analytical performance in SPR virus sensing [8].

In this work, nanoMIP receptors were exploited to develop a plasmonic sensor for the detection of the SARS-CoV-2 RBD at ultralow concentrations. Soft nanoMIP recognition elements were designed to realize a highly sensitive and portable SPR platform. The proposed RBD sensor highlights the advantages of nanoMIPs in terms of specificity, affinity, and sensitivity enhancement, resulting in improved overall biosensing performance. The obtained results indicate that the analytical sensitivity and selectivity of the SPR–nanoMIPs sensor are suitable for RBD detection at the femtomolar level in buffer.

2. Materials and Methods

2.1. Chemicals

Acrylamide (Aam), methacrylic acid (MAA), N-tert-butylacrylamide (TBAm), N,N′-methylene bisacrylamide (BIS), N,N,N′,N′-tetramethyl ethylenediamine (TEMED), ammonium persulfate (APS), (R)-α-lipoic acid, 1-ethyl-3-(-3-dimethylaminopropyl) carbodiimide hydrochloride (EDC), N-hydroxysuccinimide (NHS), Tris-HCl, Trypsin-TPCK, Trizma, (R)-α-lipoic acid, 1-ethyl-3-(-3-dimethylaminopropyl) carbodiimide hydrochloride (EDC), N-hydroxysuccinimide (NHS), 2-Morpholinoethanesulfonic acid (MES), Phosphate Buffered Saline (PBS), and Tris (hydroxymethyl)-aminomethane (TRIS) were from Sigma-Aldrich (Darmstadt, Germany). The human serum albumin (HSA) and cytochrome c proteins were from Sigma-Aldrich (Darmstadt, Germany). RBD Tris-HCl was from Excellgene (Monthey, Switzerland).

2.2. Synthesis of RBD-NanoMIPs

RBD-nanoMIPs were prepared from a monomer mixture with an overall concentration of 0.2% (*w*/*v*), in which Aam, MAA and TBAm were present at a molar ratio of 8:8:4 and combined with BIS (80% mol/mol) in 50 mM phosphate buffer (pH 7.4). The template, RBD, was added to the polymerization solution at a final concentration of 1 mg/mL. Vials were closed with rubber caps and bubbled with N_2 for 15 min. Polymerization was initiated by the addition of APS (0.04% *w*/*v*) and TEMED (0.03% *w*/*v*), and allowed to proceed for 20 h at 20 °C. Upon completion of the polymerization, the template was removed by the addition of 150 µL of 1.5 M Tris-HCl pH 8.8 and 80 µL of Trypsin-TPCK 2 mg/mL for 2 h at RT. Subsequently, 500 µL of 1 M Trizma base was added and the mixture was incubated for an additional hour. The resulting RBD-nanoMIPs were then extensively dialyzed (MWCO 10 kDa, Sigma-Aldrich, Darmstadt, Germany) against 3 L of Milli-Q water, freeze-dried and stored at −20 °C. A polymerization yield of 85% was obtained, based on the weight of lyophilized nanoparticles compared to the overall mass of monomers used during the synthesis.

2.3. Dynamic Light Scattering of NanoMIPs-RBD

Dynamic light scattering (DLS) analyses were carried out using a Zetasizer Nano ZEN3600 instrument (Malvern Instruments Ltd., Malvern, UK) equipped with a 633 nm He-Ne laser and operating at a backscattering angle of 173°. Samples were prepared by dispersing the RBD-nanoMIPs in water or PBS to a final concentration of 1 mg/mL prior to analysis. For data acquisition, a material refractive index of 1.490 and an absorption coefficient of 0.01 were applied. The dispersant properties were set according to the instrument software (Zetasizer v6.32), using an RI of 1.332 and a viscosity of 0.89 cP for water. Measurements were carried out at 298 K, and each sample was analyzed in triplicate to obtain size distribution and polydispersity index (PDI) values.

2.4. Scanning Electron Microscopy

Scanning Electron Microscopy (SEM) images were acquired using Supra 40 Field Emission Microscope (Zeiss, Oberkochen, Germany), equipped with a secondary electron detector, at a beam energy of 15 keV. Samples were prepared by dispersing the RBD-nanoMIPs in ultrapure water (150 µg/mL) and briefly ultrasonicated prior to imaging. A 5 µL aliquot of the suspension was then placed onto a silicon wafer mounted with carbon double tape on an aluminum stub. Samples were dried either at 60 °C for 24 h or at 30 °C for 72 h. To ensure adequate surface conductivity during observation, an ultrathin (≈2 nm) platinum/palladium layer was applied by plasma sputter coating.

2.5. Isothermal Titration Calorimetry

Isothermal titration calorimetry (ITC) measurements were performed using a MicroCal PEAQ-ITC instrument (Malvern Panalytical Ltd., Worcestershire, UK). All solution samples were filtered and degassed before analysis. RBD-nanoMIPs, RBD, HSA, and Cyt C were prepared in 10 mM PBS pH 7.4. For each experiment, 200 µL of RBD-nanoMIPs at 2.5 µM was titrated at 25 °C with 18 µM of RBD, 30 µM of HSA and 30 µM of Cyt C, and the corresponding heat signals were recorded. Dilution heats were determined by titrating the proteins into buffer alone. Raw injection heats were corrected by subtracting the dilution baseline and subsequently integrated. The resulting integrated heats were plotted against the molar ratio of titrant to titrand and analyzed using a one-set-of-sites binding model implemented in MicroCal PEAQ-ITC Analysis Software (version 1.22.1293). The binding constant (K_D) and the enthalpy change associated with complex formation (ΔH) were derived from fitting the calorimetric isotherms.

2.6. Portable Surface Plasmon Resonance

Surface Plasmon Resonance (SPR) measurements were carried out using a portable Spectra340 instrument (Moresense S.r.l., Milan, Italy), shown in Figure 1 [34]. The system is based on a modified D-shaped plastic optical fiber (POF) (model RA1008, Moresense S.r.l., Milan, Italy), interfaced with the reader by means a custom-designed 3D-printed holder. The optical setup consists of a VIS spectrometer operating in the 500–730 nm range and a white light source covering 400–780 nm. SPR spectra were acquired and processed using the manufacturer's dedicated software (Capture Spectrum Data, version 2.4.8).

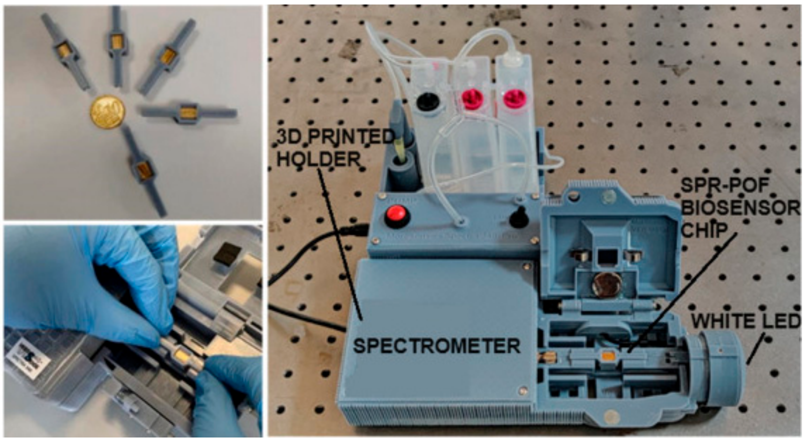

Figure 1. Picture of portable POF-SPR platform. Reprinted with permission from [34].

2.7. Functionalization of D-Shaped Plastic Optical Fiber (POF)

The gold-coated D-shaped POF surface [35] was first subjected to plasma cleaning and subsequently incubated overnight at room temperature (RT) with 0.3 mM α-lipoic acid prepared in 8% ethanol, allowing the formation of a self-assembled monolayer (SAM). Surface activation was then performed through a two-step EDC/NHS coupling procedure. Initially, 100 µL of EDC (20 mM in 50 mM MES buffer, pH 5.5) was applied for 30 min at RT. In parallel, NHS (20 mM in 50 mM MES, pH 5.5) was mixed with RBD-nanoMIPs (1 mg/mL) and allowed to react for 10 min at RT. Subsequently, 100 µL of this NHS/RBD-nanoMIPs solution was deposited onto the activated gold surface and incubated for 2 h at RT. Finally, the EDC/NHS reaction was blocked by the addition of TRIS-free base for 10 min [30]. Then, the functionalized POF was rinsed with MilliQ water and kept in MilliQ water ON at RT to remove all non-reacted materials. SAM formation and RBD-nanoMIPs immobilization were evaluated by monitoring plasmonic wavelength variations at each step, which were computed in relation to the bare POF.

2.8. RBD-NanoMIPs-POF-SPR Sensor Response to RBD

Dose–response curves for the RBD-nanoMIPs-POF-SPR sensor were generated by exposing the functionalized POF to RBD solutions prepared in PBS (10 mM, pH 7.4) at concentrations ranging from 1 fM to 1 pM. For each measurement, 100 µL of the RBD solution at the selected concentration was deposited onto the functionalized POF. SPR spectra were recorded every 3 min over a total incubation time of 15 min. Between consecutive concentrations, the surface was gently rinsed three times with PBS to remove residual analyte. SPR spectra were normalized by dividing the transmitted signal by a reference spectrum acquired in air. The absolute resonance wavelength shift ($|\Delta\lambda|$) for each RBD concentration (c) was calculated relative to the blank (i.e., buffer without analyte) using the expression $|\Delta\lambda| = \lambda_c - \lambda_0$, where λ_c is the resonance wavelength measured at concentration c, and λ_0 is the resonance wavelength of the blank. The resulting dataset was fitted using a Hill equation model, described by Equation (1):

$$\lambda = \lambda_{max} \frac{c^n}{(EC_{50} + c^n)} \tag{1}$$

where λ is the wavelength at concentration c of the ligand; λ_{max} is the value at binding saturation; n is the Hill parameter, which correlates with the number of binding sites; EC_{50} is the half-maximal effective concentration that represents the analyte concentration that produces 50% of the maximum measurable signal. OriginPro software (version 9.0, Origin Lab. Corp., Northampton, MA, USA) was used for the fitting.

2.9. Selectivity Test

The selectivity of the RBD-nanoMIPs-POF-SPR sensor was assessed using HSA and Cyt C as non-target proteins. For each experiment, 100 µL of HSA or Cyt C solutions at concentrations ranging from 1 fM to 1 pM was deposited onto the RBD-nanoMIPs-functionalized POF. Measurements and data analysis were performed following the same procedure described in the "NanoMIPs-POF-SPR Sensor Response to RBD" section.

3. Results

3.1. Synthesis and Characterization of RBD-NanoMIPs

RBD-nanoMIPs were synthesized using a total monomer concentration of 0.2% *w*/*v*. Aam, MAA and tBAm were admixed to BIS, acting as a reticulating agent. RBD (1 mg/mL) was selected as a template and added to the pre-polymerization mixture (V_{final} 10 mL) [29,36].

The RBD-nanoMIPs' dimensions were estimated by means of DLS (Figure 2A). The averaged hydrodynamic size of the nanoparticles resulted in 200 ± 19 nm, while the PDI was 0.246, indicating a fairly homogeneous distribution. As confirmation, Figure 2B presents the SEM image of the RBD-nanoMIPs, which shows spherical nanoparticles with dimensions in agreement with the DLS data.

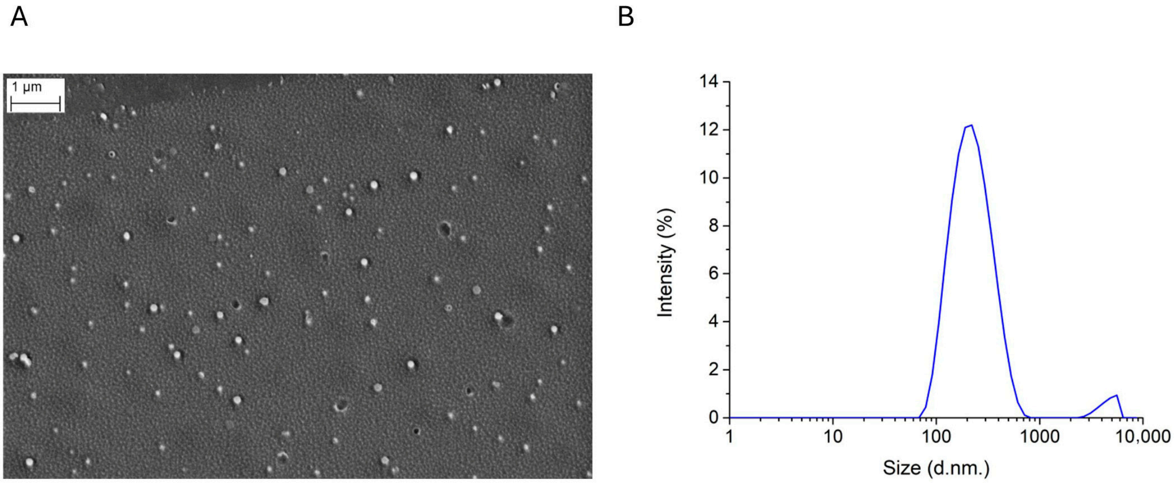

Figure 2. (**A**) Exemplificative SEM image of RBD-nanoMIPs; (**B**) DLS by intensity distribution profile of RBD-nanoMIPs.

Isothermal titration calorimetry (ITC; Figure 3) was employed to evaluate the recognition properties of RBD-nanoMIPs towards their putative ligand, RBD. This technique detects the heat exchanges associated with complex formation, providing thermodynamic information on the interaction between the analyte and nanoparticles. In this experiment, 2.5 μM of RBD-nanoMIPs was titrated in 12 sequential injections of a solution of RBD template or non-related proteins, such as human serum albumin (HSA) or cytochrome C (Cyt C). The heat generated upon each injection was recorded, integrated, and corrected by subtracting the heat of dilution contribution (i.e., the heat of the injectant titrated into pure buffer). The corrected heat areas, expressed in kJ/mol, were plotted as a function of the molar ratio between titrand and injectant and subsequently fitted using a one-set-of-sites binding model equation.

Table 1. Thermodynamic parameters obtained from the nanocalorimetric titrations of RBD nanoMIPs with RBD and HAS. Data were fitted via an independent binding site model equation.

Titrand	**Titrant**	***n***	**K_D (μM)**	**ΔH (kcal/mol)**	**ΔG (kcal/mol)**
RBD 18 μM	RBD nanoMIPs 2.5 μM	0.88 ± 0.20	0.285 ± 0.100	−110	−37.4
HSA 30 μM	RBD nanoMIPs 2.5 μM	3.76 ± 1.58	4.93 ± 3.30	414	−30.3

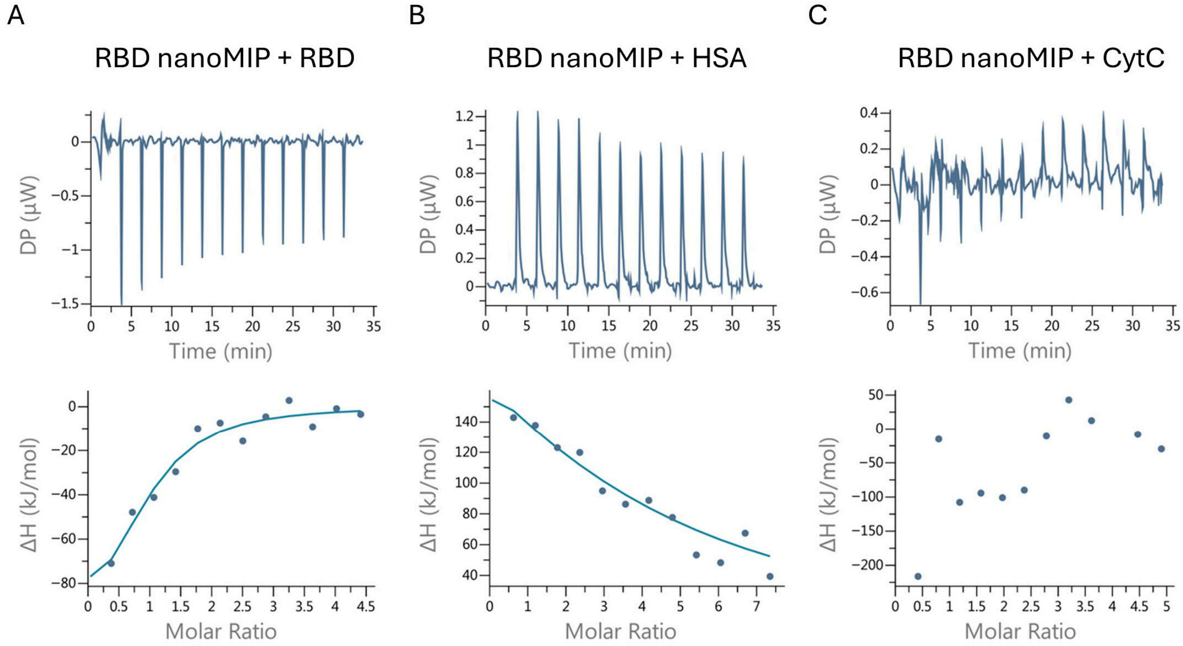

Figure 3. Energetics of the interaction between RBD-nanoMIPs and (**A**) RBD, or (**B**) HSA, or (**C**) CytC. Upper panel: heats associated with the interactions recorded over time. Lower panel: heat contributions integrated and plotted as a function of the molar ratio RBD-nanoMIPs/titrant (filled dots). Fittings with a single point equation are plotted as a line. Enthalpic-driven interactions are observed for RBD-nanoMIPs and RBD (**A**). Entropic-driven interactions are observed for RBD-nanoMIP and HSA (**B**). No interactions are observed for RBD-nanoMIPs and CytC (**C**). Fitting parameters are reported in Table 1. Data are the mean value of triplicates.

The titration of RBD nanoMIPs with their template, RBD, resulted in negative heat exchanges with a typical saturation course (Figure 3A), suggesting a target-specific enthalpically driven interaction. Instead, the titration of RBD nanoMIPs with the non-template protein HSA showed an entropically driven interaction, given by the positive heat contributions (Figure 3B), and a quasi-saturation course, which could be ascribed to the non-specific adsorption properties of HSA. Finally, no clear trend was observed for RBD nanoMIPs titrated with Cyt C (Figure 3C). As Cyt C is a highly charged protein characterized by a pI of 10.6, this suggested the establishment of only weak non-specific interactions.

The analysis of the thermograms allowed the estimation of the binding constant and the thermodynamic parameters, according to [37,38], for the RBD nanoMIPs/RBD pair, and the results were compared with those estimated for the RBD nanoMIPs/HSA pair. Data are reported in Table 1.

The RBD nanoMIPs/RBD interaction was confirmed to be a spontaneous enthalpy-driven process, having a negative Gibbs free energy variation. The estimated dissociation constant (K_D) was $2.85 \pm 1.10 \times 10^{-9}$ M. The average number of binding sites per particle (n) estimated for RBD recognition was close to 1. In contrast, the K_D estimated for HSA was 4.93×10^{-6} M, indicating 3 orders of magnitude weaker preference of RBD nanoMIPs for serum albumin. The non-specificity of the interaction was also supported by the high n number (Table 1) estimated for the RBD nanoMIPs/HSA pair, suggesting multiple weak interactions.

Figure 4 reports the estimated energetic contributions given by the software of ITC Malvern for the RBD nanoMIPs/RBD pair (Figure 4A) in comparison to those for the RBD nanoMIPs/HSA pair (Figure 4B).

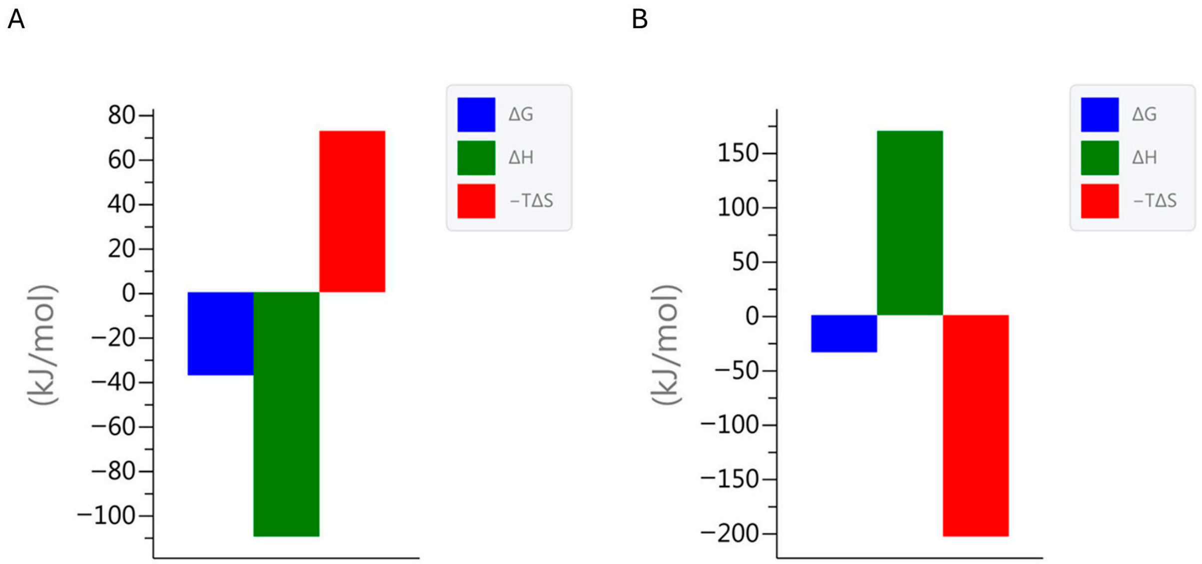

Figure 4. Thermodynamic contributions derived from ITC measurements for the interaction between RBD-nanoMIPs and (**A**) the RBD template and (**B**) the non-template protein HSA. The bar plots report the Gibbs free energy change (ΔG, blue), enthalpy change (ΔH, green) and the entropic contribution (−TΔS, red). Representative graph. Standard deviation calculated on three different independent measurements was 10%.

It is evident that enthalpy drives the template-nanoMIPs interaction, indicating the formation of weak bonds between the RBD nanoMIPs/RBD pair, whereas HSA interacts with the nanoMIPs mainly by a possible desolvation mechanism, which is entropically driven. Overall, these data demonstrate the success of the imprinting of RBD-peptide in RBD nanoMIPs and supports the selectivity of the formed recognition nanomaterials.

3.2. Preparation of the RBD-NanoMIPs-POF-SPR Sensor

In this work, RBD-nanoMIPs were utilized to develop a portable POF-SPR sensor for the detection of the RBD domain. For this purpose, the gold-coated POF surface was functionalized with RBD-nanoMIPs, as schematically illustrated in Figure 5. Firstly, SAM was formed on the gold surface using α-lipoic acid [39]. The carboxyl groups of the SAM were then activated via EDC chemistry, followed by deposition of an NHS/RBD-nanoMIPs mixture, enabling covalent immobilization via stable amide bonds. Finally, any remaining activated sites were blocked with Tris-free base to minimize non-specific adsorption [30].

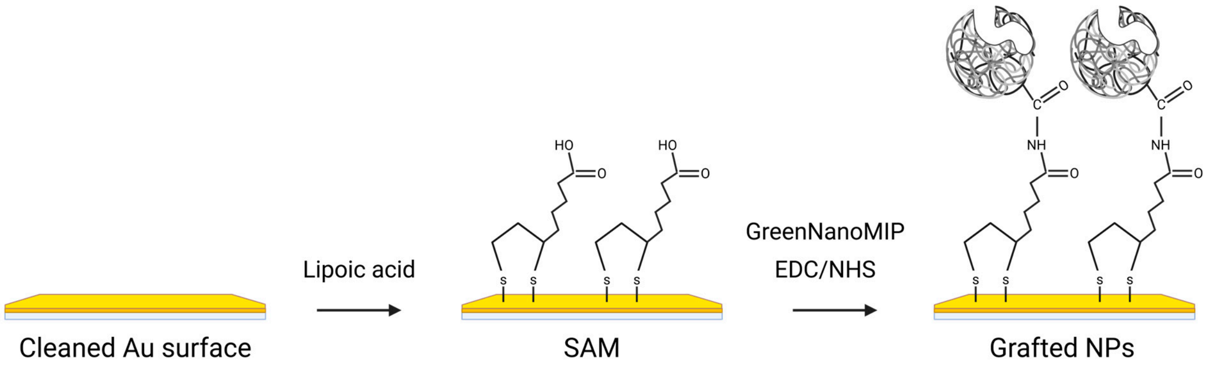

Figure 5. Schematic representation of the functionalization steps of the gold-coated POF surface with RBD-nanoMIPs. Figure reprinted/adapted from [40].

The success of the surface functionalization was evaluated by monitoring the variations in the plasmonic resonance wavelength (|Δλ|) relative to the bare probe (i.e., bare gold surface). The bare gold surface (n = 10) displayed an initial resonance at 606.32 ± 1.32 nm. After the formation of the α-lipoic acid SAM, a red shift to 610.38 ± 1.55 nm was detected, confirming effective monolayer assembly. Subsequent immobilization of the RBD-nanoMIPs induced an additional shift to 613.21 ± 1.42 nm, in line with the expected increase in thickness and refractive index at the interface resulting from the polymer coating.

This functionalization workflow was repeated on multiple POFs to assess the reproducibility of the surface modification. Figure 6 illustrates the plasmonic wavelength shifts associated with each functionalization step. In particular, SAM formation with α-lipoic acid resulted in a $|\Delta\lambda|$ of 4.06 ± 0.20 nm, which increased to 6.89 ± 0.20 nm upon immobilization of the RBD-nanoMIPs.

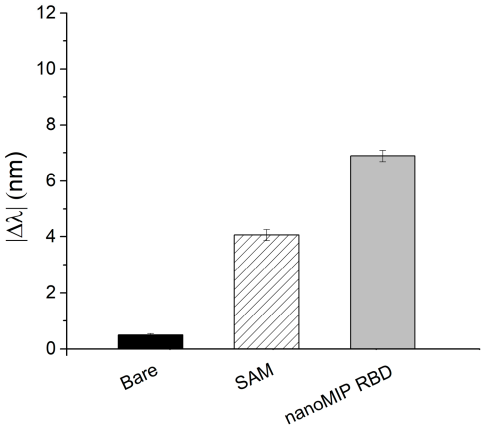

Figure 6. Absolute plasmonic resonance wavelength shifts ($|\Delta\lambda|$) of the POF-SPR after each functionalization step for the immobilization of RBD-nanoMIPs: solid black bar indicates bare gold; striped bar indicates SAM; grey bar indicates RBD-nanoMIPs.

3.3. RBD-NanoMIPs-POF-SPR Sensor Response to RBD

Prior to evaluating the binding performance of the RBD-nanoMIPs-POF-SPR sensor, the temporal stabilization of the plasmonic response was investigated in order to determine an appropriate measurement time. The resonance wavelength shift was monitored at different incubation times (0, 3, 5, and 10 min), as shown in Figure 7C. The signal rapidly increased within the first few minutes and reached a stable plateau already after 3 min of incubation, with no significant additional variation observed at longer times. This fast stabilization indicates rapid binding kinetics between the RBD and the nanoMIPs' recognition layer and supports the feasibility of short measurement times. The binding performance of the RBD-nanoMIPs-POF-SPR sensor was then evaluated in PBS using RBD concentrations ranging from 1 fM to 1 pM. The plasmonic spectra acquired after 10 min of incubation at increasing RBD concentrations are shown in Figure 7A. A progressive, concentration-dependent red shift of the resonance wavelength was observed, with values ranging from 614.42 to 619.86 nm. This behavior reflects an increase in the local refractive index at the gold surface induced by the interaction between RBD and the immobilized RBD-nanoMIPs. Binding data were analyzed using the Hill equation model (Figure 7B), and the extracted fitting and sensor parameters are summarized in Table 2. Specifically, the sensor exhibited a maximum $|\Delta\lambda|$ of approximately 5.44 nm, with half-saturation (EC_{50}) occurring at 4.99×10^{-15} M. The Hill coefficient n was 1.07, suggesting that, although RBD-nanoMIPs may contain multiple imprinted cavities, only one binding site per nanoparticle appears to be effectively accessible or to significantly contribute to the sensor response under the experimental conditions. Regarding analytical performance, the RBD-nanoMIPs-POF-SPR sensor showed a limit of detection (LOD) of 1.10×10^{-16} M, a limit of quantification (LOQ) of 3.66×10^{-16} M, and a sensitivity at low concentrations of

1.09×10^{15} nm/M. The LOD and LOQ values demonstrate outstanding sensitivity for the sensor, indicating the potential to detect SARS-CoV-2 in the attomolar range.

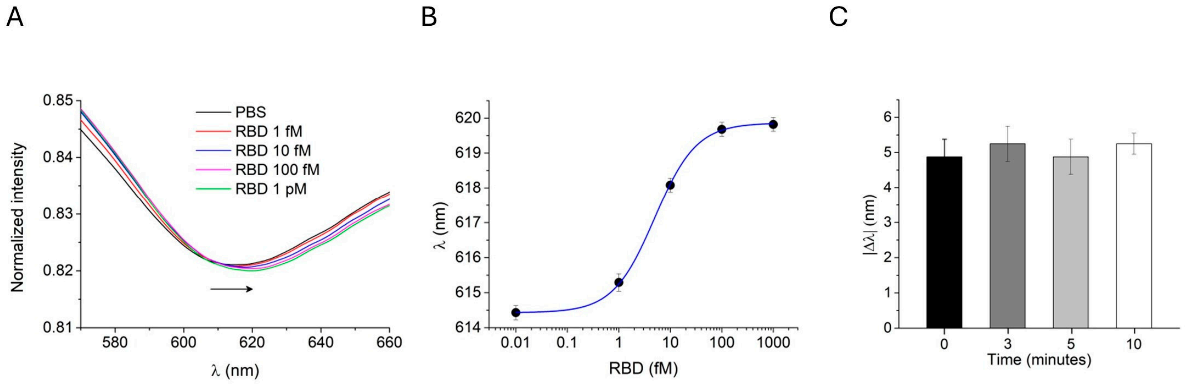

Figure 7. (**A**) Plasmonic spectra of RBD-nanoMIPs-POF-SPR sensor incubated with increased concentrations of RBD (from 1 fM to 1 pM). The arrow indicates the direction of the red-shift upon addition of the analyte. (**B**) Binding curve obtained by plotting the plasmonic wavelength shift ($|\Delta\lambda|$) as a function of RBD concentration. Experimental data points were fitted using the Hill equation model (blue line). (**C**) Time-dependent evolution of the plasmonic response, expressed as $|\Delta\lambda|$, measured at 0, 3, 5 and 10 min of incubation for a representative RBD concentration (i.e., 10 fM).

Table 2. Fitting parameters and sensor parameters related to the RBD-nanoMIPs-POF-SPR sensor's response to RBD.

Parameters	Value	
$\lambda_{\_min}$ (nm)	614.42 ± 0.04	
$\lambda_{\_max}$ (nm)	619.86 ± 0.04	
EC_{50} (M)	$4.99 \pm 0.35 \times 10^{-15}$	
n	1.07 ± 0.06	
R^2_{adj}	0.9996	
X^2_{red}	0.1875	
Sensitivity at low concentration (nm/M)	1.09×10^{15}	$\lvert \lambda_{\_max} - \lambda_{\_min} \rvert / EC_{50}$
LOQ (M)	3.66×10^{-16}	$10 \times \text{St.Dev.}_{\text{blank}}/\text{Sensitivity}_{\text{low conc}}$ *
LOD (M)	1.10×10^{-16}	$3 \times \text{St.Dev.}_{\text{blank}}/\text{Sensitivity}_{\text{low conc}}$ *

* St.Dev. blank represents the standard deviation measured when buffer is added to the sensor.

A comparison with previously reported MIP-based sensors highlights the advantages of the nanoMIP strategy adopted in this work. Cennamo et al. [31] reported an SPR sensor based on a planar MIP nanolayer targeting the S1 subunit of the SARS-CoV-2 spike protein, achieving a limit of detection of 0.058 µM, several orders of magnitude higher than the attomolar LOD obtained here. This difference can be attributed to the intrinsic limitations of continuous MIP layers, in which a significant fraction of binding sites may be buried within the polymer matrix and weakly coupled to the evanescent plasmonic field.

More advanced planar architectures have been proposed by Bognár et al. [33], who developed epitope-imprinted MIP microarrays on gold SPR imaging chips using surface imprinting and oriented template immobilization. Although strong affinities in the nanomolar range were reported for RBD recognition, the sensor performance remains constrained by the planar nature of the recognition layer. Overall, these comparisons underline how the use of nanoMIPs as discrete recognition elements provides a decisive advantage in terms of sensitivity, owing to their high surface-to-volume ratio.

3.4. Selectivity of RBD-NanoMIPs-POF-SPR Sensor

The selectivity of the RBD-nanoMIPs-POF-SPR sensor was assessed by using Cyt C and HSA as non-target proteins. The selection of these proteins was motivated by their high abundance in human plasma and their relevance as potential interfering species in complex biological samples. When tested at concentrations ranging from 1 fM to 1 pM, neither Cyt C nor HSA produced appreciable resonance wavelength shifts (Figure 8), indicating negligible non-specific interactions and confirming the high selectivity of the sensor toward RBD.

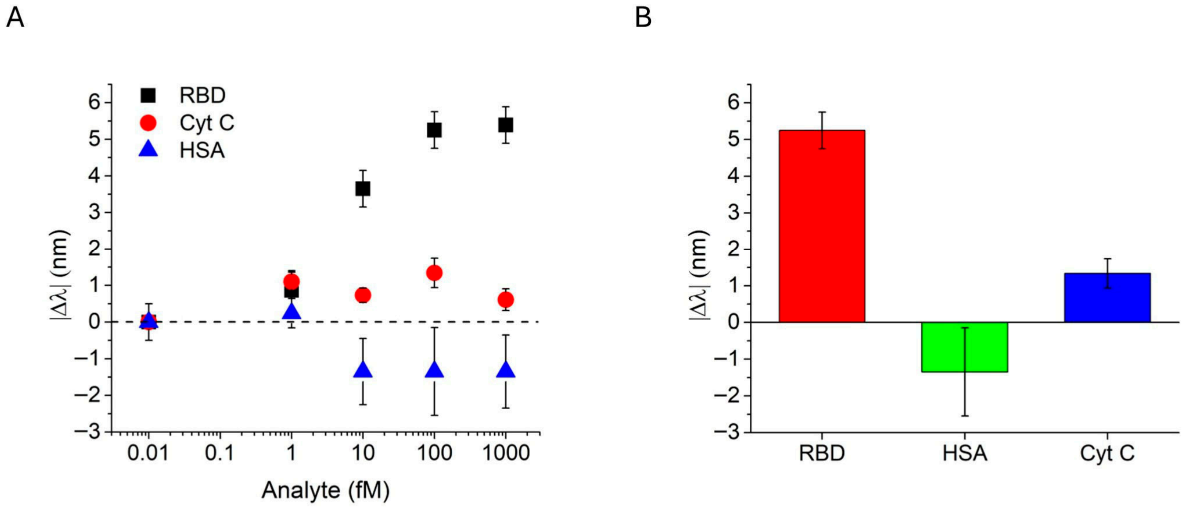

Figure 8. (**A**) Plasmonic resonance wavelength shifts (Δλ) as a function of protein concentrations for RBD (black square), Cyt C (red circles) and HSA (blue triangles). (**B**) Comparison of the plasmonic resonance wavelength shifts (Δλ) of RBD-nanoMIPs-POF-SPR sensor incubated with 100 fM of RBD (red bar), HSA (green bar) and Cyt C (blue bar).

As shown in Figure 8A, a clear concentration-dependent response was observed exclusively for RBD (black squares), whereas only minimal signal variations were recorded for Cyt C (red circles) and HSA (blue triangles) across the entire investigated range.

A comparative visualization of the sensor response at a fixed concentration of 100 fM is reported in Figure 8B. Under these conditions, RBD induced a pronounced wavelength shift of 5.25 nm, while substantially smaller responses were measured for HSA and Cyt C, −1.34 nm and 1.35 nm, respectively. The negligible positive or negative wavelength shifts observed for non-target proteins indicate the absence of effective binding interactions, with the recorded variations attributable to minor baseline fluctuations or weak, non-specific interfacial effects at the nanoMIPs layer rather than to bulk refractive index changes or specific binding events.

These results demonstrate the sensor's capability to effectively discriminate the target analyte from abundant plasma proteins, even at ultra-low concentrations.

3.5. Regeneration and Reuse of the NanoMIPs-POF-SPR Sensor

The regeneration capability of the sensor was assessed by reusing the same nanoMIPs-POF-SPR sensor over multiple days. After each binding experiment, nanoMIPs-functionalized POF was incubated in CHES buffer (20 mM) for 30 min at room temperature, followed by rinsing in Milli-Q water for 2 h.

As shown in Figure 9, the resonance wavelength measured in PBS was consistently recovered after each regeneration process, remaining within a narrow range (variation below ~1 nm) across different days. These results indicate that the proposed regeneration protocol enables effective removal of the bound analyte while preserving its selectivity.

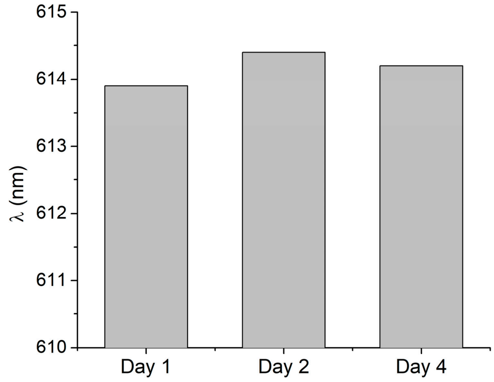

Figure 9. Resonance wavelength measured in PBS for the same nanoMIPs-functionalized POF over four consecutive days after the regeneration step.

4. Discussion

In this work, a surface plasmon resonance sensor based on plastic optical fiber functionalized with RBD-imprinted nanoMIPs was developed and investigated for the detection of the receptor binding domain. The experimental results demonstrate that the proposed sensing platform is capable of detecting the target analyte at ultra-low concentrations, as reflected by the femtomolar-range EC_{50}, and has excellent analytical performance, with limits of detection and quantification in the sub-femtomolar range.

In addition to its high sensitivity, the sensor showed a rapid response, with stable plasmonic signals reached within a few minutes, and a high degree of selectivity against potentially interfering plasma proteins. These features, combined with the use of nanoMIPs as robust and synthetic recognition elements and the intrinsic advantages of the SPR-POF configuration, such as compactness, low cost, and ease of use, make the proposed sensor a promising tool for addressing the increasing demand for rapid, early-stage, and accurate detection strategies.

Author Contributions: Conceptualization, A.M.B., J.B. and A.M.; methodology, A.M.B., A.M. and J.B.; validation, A.M. and J.B.; formal analysis, A.M.B., A.M. and J.B.; investigation, A.M.B., A.M., J.B. and D.M.; resources, A.M.B.; data curation, A.M. and J.B.; writing—original draft preparation, A.M.B., A.M. and J.B.; writing—review and editing, A.M.B., A.M. and J.B.; visualization, A.M. and J.B.; supervision, A.M.B. and D.M.; project administration, A.M.B. and D.M.; funding acquisition, A.M.B. and D.M. All authors have read and agreed to the published version of the manuscript.

Funding: This research was funded by Bando COVID-19 of the University of Trento; Italian Ministry of Research and University doctoral program PON PNRR DM351.

Institutional Review Board Statement: Not applicable.

Informed Consent Statement: Not applicable.

Data Availability Statement: The data are available on reasonable request from the corresponding author.

Acknowledgments: A.M.B. and D.M acknowledge the Bando COVID-19 of the University of Trento for the OPTOVIR project; A.M.B. acknowledges the Centro Piattaforme Tecnologiche (CPT) of the University of Verona for the facilities DLS and ITC. The authors are grateful to Massimo Pizzato from CIBIO, University of Trento, for the insightful discussion.

Conflicts of Interest: The authors declare no conflicts of interest. The funders had no role in the design of the study; in the collection, analyses, or interpretation of data; in the writing of the manuscript; or in the decision to publish the results.

Abbreviations

The following abbreviations are used in this manuscript:

NanoMIPs	Molecularly imprinted polymer nanoparticles
RBD	Receptor-binding domain
SPR	Surface plasmon resonance
POF	Plastic optical fiber

References

1. Zhou, P.; Yang, X.L.; Wang, X.G.; Hu, B.; Zhang, L.; Zhang, W.; Si, H.R.; Zhu, Y.; Li, B.; Huang, C.L.; et al. A pneumonia outbreak associated with a new coronavirus of probable bat origin. *Nature* **2020**, *579*, 270–273. [CrossRef] [PubMed]
2. Walls, A.C.; Park, Y.J.; Tortorici, M.A.; Wall, A.; McGuire, A.T.; Veesler, D. Structure, Function, and Antigenicity of the SARS-CoV-2 Spike Glycoprotein. *Cell* **2020**, *183*, 1735. [CrossRef] [PubMed]
3. Shang, J.; Ye, G.; Shi, K.; Wan, Y.; Luo, C.; Aihara, H.; Geng, Q.; Auerbach, A.; Li, F. Structural basis of receptor recognition by SARS-CoV-2. *Nature* **2020**, *581*, 221–224. [CrossRef] [PubMed]
4. Corman, V.M.; Landt, O.; Kaiser, M.; Molenkamp, R.; Meijer, A.; Chu, D.K.; Bleicker, T.; Brunink, S.; Schneider, J.; Schmidt, M.L.; et al. Detection of 2019 novel coronavirus (2019-nCoV) by real-time RT-PCR. *Eurosurveillance* **2020**, *25*, 2000045. [CrossRef]
5. Vashist, S.K. In Vitro Diagnostic Assays for COVID-19: Recent Advances and Emerging Trends. *Diagnostics* **2020**, *10*, 202. [CrossRef]
6. Carter, L.J.; Garner, L.V.; Smoot, J.W.; Li, Y.; Zhou, Q.; Saveson, C.J.; Sasso, J.M.; Gregg, A.C.; Soares, D.J.; Beskid, T.R.; et al. Assay Techniques and Test Development for COVID-19 Diagnosis. *ACS Cent. Sci.* **2020**, *6*, 591–605. [CrossRef]
7. Kevadiya, B.D.; Machhi, J.; Herskovitz, J.; Oleynikov, M.D.; Blomberg, W.R.; Bajwa, N.; Soni, D.; Das, S.; Hasan, M.; Patel, M.; et al. Diagnostics for SARS-CoV-2 infections. *Nat. Mater.* **2021**, *20*, 593–605. [CrossRef]
8. Bajaj, A.; Trimpert, J.; Abdulhalim, I.; Altintas, Z. Synthesis of Molecularly Imprinted Polymer Nanoparticles for SARS-CoV-2 Virus Detection Using Surface Plasmon Resonance. *Chemosensors* **2022**, *10*, 459. [CrossRef]
9. Pitruzzella, R.; Rovida, R.; Arcadio, F.; Marzano, C.; Passeggio, F.; Pasquardini, L.; D'Agostino, G.; Zeni, L.; Portella, G.; Cennamo, N. Towards SARS-CoV-2 detection at six orders of magnitude lower than RT-PCR via nanoplasmonic probes and MIPs. *Microchem. J.* **2025**, *216*, 114695. [CrossRef]
10. Wang, Q.; Cao, Y.; Yuan, Z.; Han, M.; Zhang, Y.; Zhuo, K.; Sun, L.; Guo, X.; Zhang, H.; Jin, H. Magnetoelastic Immunosensor for the Rapid Detection of SARS-CoV-2 in Bioaerosols. *ACS Sens.* **2024**, *9*, 5936–5944. [CrossRef]
11. Nguyen, H.H.; Park, J.; Kang, S.; Kim, M. Surface Plasmon Resonance: A Versatile Technique for Biosensor Applications. *Sensors* **2015**, *15*, 10481–10510. [CrossRef] [PubMed]
12. Masson, J.F. Surface Plasmon Resonance Clinical Biosensors for Medical Diagnostics. *ACS Sens.* **2017**, *2*, 16–30. [CrossRef] [PubMed]
13. Djaileb, A.; Charron, B.; Jodaylami, M.H.; Thibault, V.; Coutu, J.; Stevenson, K.; Forest, S.; Live, L.S.; Boudreau, D.; Pelletier, J.N.; et al. A Rapid and Quantitative Serum Test for SARS-CoV-2 Antibodies with Portable Surface Plasmon Resonance Sensing. *Anal. Methods* **2021**, *13*, 1694–1701.
14. Abboud, R.; Mirzanejhad, S.; Jouybari, S.N.; Eshghabadi, M. Surface plasmon resonance of nanometer Ag-Cu alloy layers on Blu-ray and DVD disks. *Sens. Actuators A-Phys.* **2025**, *391*, 116660. [CrossRef]
15. Perera, G.S.; Rahman, M.A.; Blazevski, A.; Wood, A.; Walia, S.; Bhaskaran, M.; Sriram, S. Rapid Conductometric Detection of SARS-CoV-2 Proteins and Its Variants Using Molecularly Imprinted Polymer Nanoparticles. *Adv. Mater. Technol.* **2022**, *8*, 2200965. [CrossRef]
16. Trzaskowski, M.; Mazurkiewicz-Pisarek, A.; Trzcinski, J.W.; Drozd, M.; Podgorski, R.; Zabost, A.; Augustynowicz-Kopec, E. Portable Surface Plasmon Resonance Detector for COVID-19 Infection. *Sensors* **2023**, *23*, 3946. [CrossRef]
17. McClements, J.; Bar, L.; Singla, P.; Canfarotta, F.; Thomson, A.; Czulak, J.; Johnson, R.E.; Crapnell, R.D.; Banks, C.E.; Payne, B.; et al. Molecularly Imprinted Polymer Nanoparticles Enable Rapid, Reliable, and Robust Point-of-Care Thermal Detection of SARS-CoV-2. *ACS Sens.* **2022**, *7*, 1122–1131. [CrossRef]
18. Pandey, P.S.; Raghuwanshi, S.K.; Shadab, A.; Ansari, M.T.I.; Tiwari, U.K.; Kumar, S. SPR Based Biosensing Chip for COVID-19 Diagnosis—A Review. *IEEE Sens. J.* **2022**, *22*, 13800–13810. [CrossRef]

19. Ayankojo, A.G.; Boroznjak, R.; Reut, J.; Öpik, A.; Syritski, V. Molecularly imprinted polymer based electrochemical sensor for quantitative detection of SARS-CoV-2 spike protein. *Sens. Actuators B-Chem.* **2022**, *353*, 131160. [CrossRef]
20. Cennamo, N.; Pasquardini, L.; Arcadio, F.; Lunelli, L.; Vanzetti, L.; Carafa, V.; Altucci, L.; Zeni, L.G. SARS-CoV-2 spike protein detection through a plasmonic D-shaped plastic optical fiber aptasensor. *Talanta* **2021**, *233*, 122532. [CrossRef]
21. Bossi, A.; Bonini, F.; Turner, A.P.F.; Piletsky, S.A. Molecularly imprinted polymers for the recognition of proteins: The state of the art. *Biosens. Bioelectron.* **2007**, *22*, 1131–1137. [CrossRef] [PubMed]
22. Malik, M.I.; Shaikh, H.; Mustafa, G.; Bhanger, M.I. Recent Applications of Molecularly Imprinted Polymers in Analytical Chemistry. *Sep. Purif. Rev.* **2019**, *48*, 179–219. [CrossRef]
23. Haupt, K. Molecularly imprinted polymers in analytical chemistry. *Analyst* **2001**, *126*, 747–756. [CrossRef] [PubMed]
24. Haupt, K.; Rangel, P.X.M.; Bui, B.T.S. Molecularly Imprinted Polymers: Antibody Mimics for Bioimaging and Therapy. *Chem. Rev.* **2020**, *120*, 9554–9582. [CrossRef]
25. Haupt, K.; Mosbach, K. Molecularly imprinted polymers and their use in biomimetic sensors. *Chem. Rev.* **2000**, *100*, 2495–2504. [CrossRef]
26. Haupt, K. BIOMATERIALS Plastic antibodies. *Nat. Mater.* **2010**, *9*, 612–614. [CrossRef]
27. Poma, A.; Turner, A.P.F.; Piletsky, S.A. Advances in the manufacture of MIP nanoparticles. *Trends Biotechnol.* **2010**, *28*, 629–637. [CrossRef]
28. Cenci, L.; Tatti, R.; Tognato, R.; Ambrosi, E.; Piotto, C.; Bossi, A.M. Synthesis and characterization of peptide-imprinted nanogels of controllable size and affinity. *Eur. Polym. J.* **2018**, *109*, 453–459. [CrossRef]
29. Cenci, L.; Andreetto, E.; Vestri, A.; Bovi, M.; Barozzi, M.; Iacob, E.; Busato, M.; Castagna, A.; Girelli, D.; Bossi, A.M. Surface plasmon resonance based on molecularly imprinted nanoparticles for the picomolar detection of the iron regulating hormone Hepcidin-25. *J. Nanobiotechnol.* **2015**, *13*, 51. [CrossRef]
30. Cennamo, N.; Maniglio, D.; Tatti, R.; Zeni, L.; Bossi, A.M. Deformable molecularly imprinted nanogels permit sensitivity-gain in plasmonic sensing. *Biosens. Bioelectron.* **2020**, *156*, 112126. [CrossRef]
31. Cennamo, N.; D'Agostino, G.; Perri, C.; Arcadio, F.; Chiaretti, G.; Parisio, E.M.; Camarlinghi, G.; Vettori, C.; Di Marzo, F.; Cennamo, R.; et al. Proof of Concept for a Quick and Highly Sensitive On-Site Detection of SARS-CoV-2 by Plasmonic Optical Fibers and Molecularly Imprinted Polymers. *Sensors* **2021**, *21*, 1681. [CrossRef]
32. Bertolla, M.; Cenci, L.; Anesi, A.; Ambrosi, E.; Tagliaro, F.; Vanzetti, L.; Guella, G.; Bossi, A.M. Solvent-Responsive Molecularly Imprinted Nanogels for Targeted Protein Analysis in MALDI-TOF Mass Spectrometry. *ACS Appl. Mater. Inter.* **2017**, *9*, 6908–6915. [CrossRef]
33. Bognar, Z.; Supala, E.; Yarman, A.; Zhang, X.; Bier, F.F.; Scheller, F.W.; Gyurcsanyi, R.E. Peptide epitope-imprinted polymer microarrays for selective protein recognition. Application for SARS-CoV-2 RBD protein. *Chem. Sci.* **2022**, *13*, 1263–1269. [CrossRef] [PubMed]
34. Pasquardini, L.; Cennamo, N.; Arcadio, F.; Perri, C.; Chiodi, A.; D'agostino, G.; Zeni, L. Immuno-SPR biosensor for the detection of Brucella abortus. *Sci. Rep.* **2023**, *13*, 22832. [CrossRef]
35. Cennamo, N.; Massarotti, D.; Conte, L.; Zeni, L. Low Cost Sensors Based on SPR in a Plastic Optical Fiber for Biosensor Implementation. *Sensors* **2011**, *11*, 11752–11760. [CrossRef]
36. Hoshino, Y.; Kodama, T.; Okahata, Y.; Shea, K.J. Peptide imprinted polymer nanoparticles: A plastic antibody. *J. Am. Chem. Soc.* **2008**, *130*, 15242–15243. [CrossRef]
37. Prozeller, D.; Morsbach, S.; Landfester, K. Isothermal titration calorimetry as a complementary method for investigating nanoparticle–protein interactions. *Nanoscale* **2019**, *11*, 19265–19273. [CrossRef]
38. Pierce, M.M.; Raman, C.S.; Nall, B.T. Isothermal titration calorimetry of protein-protein interactions. *Methods* **1999**, *19*, 213–221. [CrossRef]
39. Pasquardini, L.; Cennamo, N.; Malleo, G.; Vanzetti, L.; Zeni, L.; Bonamini, D.; Salvia, R.; Bassi, C.; Bossi, A.M. A Surface Plasmon Resonance Plastic Optical Fiber Biosensor for the Detection of Pancreatic Amylase in Surgically-Placed Drain Effluent. *Sensors* **2021**, *21*, 3443. [CrossRef]
40. Marinangeli, A.; Hatir, P.C.; Yagci, M.B.; Bossi, A.M. Highly Sensitive Biosensor for the Detection of Cardiac Troponin I in Serum via Surface Plasmon Resonance on Polymeric Optical Fiber Functionalized with Castor Oil-Derived Molecularly Imprinted Nanoparticles. *Biosensors* **2025**, *16*, 12. [CrossRef]